

Targeting T₁ and T₂ dual modality enhanced magnetic resonance imaging of tumor vascular endothelial cells based on peptides-conjugated manganese ferrite nanomicelles

Mingfu Gong¹
Hua Yang^{1,2}
Song Zhang¹
Yan Yang¹
Dong Zhang¹
Zhaohui Li³
Liguang Zou¹

¹Department of Radiology, Xinqiao Hospital, Third Military Medical University, Chongqing, People's Republic of China; ²Department of Radiology, Chongqing Traditional Chinese Medicine Hospital, Chongqing, People's Republic of China; ³Geosciences Department, University of Wisconsin-Parkside, Kenosha, WI, USA

Abstract: Tumor angiogenesis plays very important roles for tumorigenesis, tumor development, metastasis, and prognosis. Targeting T₁/T₂ dual modality magnetic resonance (MR) imaging of the tumor vascular endothelial cells (TVECs) with MR molecular probes can greatly improve diagnostic sensitivity and specificity, as well as helping to make an early diagnosis of tumor at the preclinical stage. In this study, a new T₁ and T₂ dual modality nanoprobe was successfully fabricated. The prepared nanoprobe comprise peptides CL 1555, poly(ε-caprolactone)-block-poly(ethylene glycol) amphiphilic copolymer shell, and dozens of manganese ferrite (MnFe₂O₄) nanoparticle core. The results showed that the hydrophobic MnFe₂O₄ nanoparticles were of uniform spheroidal appearance and narrow size distribution. Due to the self-assembled nanomicelles structure, the prepared probes were of high relaxivity of 281.7 mM⁻¹ s⁻¹, which was much higher than that of MnFe₂O₄ nanoparticles (67.5 mM⁻¹ s⁻¹). After being grafted with the targeted CD105 peptide CL 1555, the nanomicelles can combine TVECs specifically and make the labeled TVECs dark in T₂-weighted MR imaging. With the passage on, the Mn²⁺ ions were released from MnFe₂O₄ and the size decreased gradually, making the signal intensity of the second and third passage of labeled TVECs increased in T₁-weighted MR imaging. Our results demonstrate that CL-poly(ethylene glycol)-MnFe₂O₄ can conjugate TVECs and induce dark and bright contrast in MR imaging, and act as a novel molecular probe for T₁- and T₂-enhanced MR imaging of tumor angiogenesis.

Keywords: CL 1555, CL-PEG-MnFe₂O₄, TVECs, CD105, tumor angiogenesis

Introduction

Malignant tumor has been ranked the second leading cause of human mortality worldwide, accounting for 8.2 million cancer deaths in 2012.¹ The lethality of cancer is mainly due to early metastasis and diagnosis at advanced stages. The common routes of metastasis of malignant tumors are hematogenous metastasis, lymphatic metastasis, implantation metastasis, and local infiltration, among which the blood metastases are the most important routes.^{2,3} In 1971, Folkman reported that the occurrence and development of a tumor were angiogenesis-dependent and tumor angiogenesis accelerated tumor growth and infiltration.⁴ So, the tumor blood vessels became the focus of cancer research, making vascular endothelial cells the leading targets for cancer research. In recent years, with the discovery of a series of markers of vascular endothelial cells, the study of tumor blood vessels has expanded into the molecular

Correspondence: Liguang Zou
Department of Radiology, Xinqiao Hospital, Third Military Medical University, No 183, Xinqiao Street, Shapingba District, Chongqing, People's Republic of China
Tel +86 23 6877 4036
Fax +86 23 6875 5306
Email cqxyyzzlg@163.com

level and the relationship between tumor blood vessels and tumor metastasis was confirmed through these molecular markers.⁵⁻⁸ Endoglin, also called CD105, is a moiety of the transforming growth factor-beta receptor complex and regulates angiogenesis by participating in signal transduction of the transforming growth factor-beta receptor. It has been reported that CD105 is overexpressed in neovascularization of regenerated, inflammatory, and tumor tissues and its expression is positively correlated with the cancer angiogenesis.⁷⁻⁹ Therefore, CD105 is an ideal biomarker for targeting tumor vascular endothelial cells (TVECs).

Magnetic resonance imaging (MRI) is one of the best noninvasive methods used in clinical medicine today because of its superb spatial resolution, soft-tissue contrast resolution, lack of radiation exposure, and multiparameter and multi-sequence imaging.¹⁰⁻¹² However, MRI is less sensitive than positron emission tomography and fluorescence imaging, making it not suitable for small lesion monitoring or molecule tracing. The application of magnetic contrast agents (CAs) markedly enhances the sensitivity of MRI.¹³⁻¹⁵ Usually, MR CAs can be divided into two categories: one is positive CAs, which can mainly reduce longitudinal relaxation (T_1) time and induce hyperintensity in T_1 -weighted imaging; the other is negative CAs which can mainly shorten transverse relaxation (T_2) time and provide negative contrast in T_2 -weighted imaging.¹⁶ There have been many types of CAs available for clinical MRI, including gadolinium- or manganese-based chelates as T_1 CAs and iron oxide (Fe_3O_4)-based nanoparticles (NPs) as T_2 CAs.¹⁷⁻¹⁹ However, both kinds of CAs have limitations. Because of magnetic susceptibility artifacts and their positive or negative contrast effect, the tissues labeled with gadolinium-based complex or Fe_3O_4 NPs may not be clearly distinguishable from the hyperintensity or low level MR signal arising from adjacent tissues.^{20,21} Meanwhile, it has been reported that some gadolinium-based CAs can result in nephrogenic systemic fibrosis for patients with severe renal disease.²² Manganese ferrite ($MnFe_2O_4$) NPs have been proven to be of higher saturation magnetization and transverse relaxivity (r_2) than other ferrite NPs, including cobalt ferrite ($CoFe_2O_4$), Fe_3O_4 , and nickel ferrite ($NiFe_2O_4$).²³⁻²⁵ Additionally, multiple $MnFe_2O_4$ NPs encapsulated inside one nanomicelle (NM) can result in much stronger r_2 than a single NP at the same metal concentration, making them excellent candidates for high sensitive T_2 -enhanced MRI.^{26,27} The $MnFe_2O_4$ NPs within cells will be gradually broken down in lysosomes and then release paramagnetic Mn^{2+} . At the mean time, the size of $MnFe_2O_4$ NPs decreased correspondingly. The above two effects can significantly shorten the T_1 relaxation time of the surrounding protons and

induce hyperintensity in T_1 -weighted imaging.^{19,28-31} So, the $MnFe_2O_4$ NPs can act as both T_1 and T_2 CAs in MRI. As a negative CA, $MnFe_2O_4$ NPs can cause dark contrast in T_2 and T_2^* -weighted imaging (WI). Upon internalization by cells and localization in lysosomes, released Mn^{2+} ions and NPs with smaller size can act as strong T_1 MRI CAs, making the dark areas in T_2/T_2^* -WI bright in T_1 -weighted imaging,^{30,32} to improve the accuracy of diagnosis of MRI greatly.

Bi³³ identified a peptide with high binding affinity and selectivity toward CD105 and demonstrated that the selected peptide could act as a CD105 specific ligand. The peptide called CL 1555 (sequence: AHKHVHHVPVRL) was selected from a phage displayed library.³⁴ CL 1555 was condensed with only a dozen of amino acids, resulting in a simpler steric configuration, better diffusion and penetration in vivo, and less immunogenicity compared with anti-CD105 antibody. Because of small steric hindrance, the peptide had a high grafting rate when it was connected to the functional group on the surface of the NPs, which will improve the probe affinity, connective stability, and specificity with the targeted molecule.³⁵ So, CL 1555 is an ideal ligand to CD105 for targeted diagnosis and therapy.

In previous studies, we conjugated anti-CD105 antibody with stabilized immunoliposome (SL)-encapsulated gadolinium-diethylenetriaminepentaacetic acid (Gd-DTPA) and thiol-PEG-carboxyl-stabilized Fe_2O_3/Au NPs to evaluate tumor angiogenesis on T_1 - or T_2 -enhanced MRI, respectively.^{36,37} The results showed that CD105-Gd-SLs and hybrid-PEG-CD105 could be utilized to detect subcutaneous glioma and breast cancer angiogenesis in tumor-bearing rats. Based on the previous work, this research focuses on synthesizing and characterizing a molecular probe CL-poly(ethylene glycol) (PEG)- $MnFe_2O_4$ based on the CD105 specific ligand CL 1555 and $MnFe_2O_4$ NMs to detect tumor angiogenesis using T_1 - and T_2 -enhanced MRI.

Materials and methods

Materials

Iron acetylacetonate, manganese acetylacetonate, oleic acid, oleylamine, benzyl ether, hexane, ϵ -caprolactone, tetrahydrofuran (THF), N-(3-dimethylaminopropyl)-N-ethylcarbodiimide, N-hydroxysuccinimide, stannous octoate, tetramethylammonium hydroxide (TMAH), heparin, L-glutamine, reactive oxygen species (ROS) assay kit, and sodium pyruvate were all purchased from Sigma-Aldrich Co. (St Louis, MO, USA). PEG with a terminal hydroxyl and carboxylic acid functional groups (COOH-PEG-OH) was purchased from JenKem Technology (Beijing, People's Republic of China). 1,2-Hexadecanediol was obtained from

TCI (Shanghai) Development Co., Ltd (Shanghai, People's Republic of China). Medium 199, Roswell Park Memorial Institute 1640 medium, fetal bovine serum, penicillin/streptomycin, and nonessential amino acid were purchased from Hyclone, Logan, UT, USA. Count Kit-8 (CCK-8) was obtained from Beyotime Biotechnology Company, Beijing, People's Republic of China. Endothelial cell growth supplement was purchased from Sciencell, CA, Carlsbad, USA. Six-well plates were obtained from Corning Incorporated, Corning, NY, USA.

Synthesis of MnFe₂O₄ NPs

According to a published procedure,³⁸ iron acetylacetonate (2 mmol), manganese acetylacetonate (1 mmol), 1,2-hexadecanediol (10 mmol), oleic acid (6 mmol), and oleylamine (6 mmol) were mixed in 20 mL benzyl ether under dry and deoxidized argon atmosphere. Then, the mixture was successively heated to 200°C for 2 hours and refluxed at 300°C for 1 hour. After cooling to room temperature, the mixture was treated with ethanol and then centrifuged several times. Finally, the product was dispersed in anhydrous hexane for storage. In order to transfer the prepared NPs into water, hydrophobic MnFe₂O₄ NPs were treated with TMAH.³⁹ Briefly, 10 mL of NPs suspension in hexane was added into 20 mL of ethanol and the NPs were collected with a permanent magnet. After decanting the solvent, the NPs were redispersed in 25 mL of TMAH aqueous solution (10%, w/v) and sonicated for 10 minutes. After centrifugation, the hydrophobic surfactant (oleic acid/oleylamine) on the surface of NPs was replaced with TMAH, making them bear negative surface charges and be stable in water. Finally, the surface ligand-exchanged NPs (TMAH-MnFe₂O₄) were suspended in 10 mL of deionized water.

Synthesis of CL-PEG-MnFe₂O₄

Amphiphilic block copolymer poly(ϵ -caprolactone)-block-PEG-COOH (PCL-*b*-PEG-COOH) was synthesized using ϵ -caprolactone, COOH-PEG-OH, and stannous octoate by ring opening polymerization.⁴⁰ The resulting copolymers were dissolved in THF and precipitated in excess amount of diethyl ether. The precipitates were then dried in vacuum oven. The dried MnFe₂O₄ NPs and prepared copolymer were redispersed in THF with a mass ratio of 2:1. Afterwards, the ultrapure water was poured into the mixture under ultrasonication. The oil-water mixture was then dialyzed in a dialysis bag with a molecular weight cutoff of 14,000 overnight to remove the residual THF and the remaining products were PEG-*b*-PCL-MnFe₂O₄ NMs. CL 1555 was purchased from ChinaPeptides Co., Ltd (Shanghai, People's

Republic of China) and coupled to terminal carboxylic acid functional amphiphilic block copolymer PCL-*b*-PEG-COOH through N-(3-dimethylaminopropyl)-N-ethylcarbodiimide/N-hydroxysuccinimide chemistry following a previous method.^{40,41} Finally, the TVECs targeting nanoprobe CL-PEG-MnFe₂O₄ NMs were obtained.

NP characterization

The morphology, size, and size distribution of MnFe₂O₄ and PEG-*b*-PCL-MnFe₂O₄ were measured using transmission electron microscopy (TEM) (JEM-2100F, JEOL, Tokyo, Japan). The diameter in dispersion and polydispersity index were determined through the dynamic light scattering technique (Nano zs90, Malvern Instruments, Malvern, UK). The Fe and Mn elemental contents of MnFe₂O₄ and PEG-*b*-PCL-MnFe₂O₄ were quantified by energy dispersive spectrometer analysis in TEM (JEM-2100F) and inductive-coupled plasma optical emission spectrometer. The coercivity, magnetization, and hysteresis loop of MnFe₂O₄ were evaluated using vibrating sample magnetometer (ADE Technologies, Lowell, MA, USA). Serial metal (Fe + Mn) concentrations (0, 0.01, 0.02, 0.03, 0.04, 0.06, 0.08, 0.1, 0.2, 0.4, 0.6, and 0.8 mM) of both TMAH-MnFe₂O₄ and PEG-*b*-PCL-MnFe₂O₄ were scanned in a head coil using a 3.0 T clinical MR scanner (Signa HDx, GE healthcare, Little Chalfont, UK). The scanning parameters were as follows: matrix 256×256, field of view 16×16 cm, interlayer spacing 0.4 mm, fast spin echo (FSE) T₂-weighted imaging (repetition time [TR] 2000 ms and echo time [TE] 43.7 ms), gradient echo [GRE] T₂*WI (TR 400 ms, TE 12.0 ms, and flip angle 30°), and 16 echo T₂ mapping (TR 1025 ms and TE 2.4–60.5 ms). The r_2 was calculated through the curve fitting of the 1/T₂ relaxation time (s⁻¹) versus the concentration (mM). The region of interest was 5 mm².

Cells culture

Human umbilical vein endothelial cells (HUVECs) were routinely harvested by digesting human umbilical veins with type-I collagenase as previously described.⁴² With approval from the Medical Ethics Committee of Xinqiao Hospital of Third Military Medical University and written patient consent, the human umbilical cords were obtained from the Department of Obstetrics and Gynecology of Xinqiao Hospital. The specificity and purity of the isolated cells were evaluated using immunofluorescence staining and flow cytometry. HUVECs were cultured in medium 199 supplemented with 20% fetal bovine serum, 1% endothelial cell growth supplement, 0.05 mg/mL of heparin, 2 mM of L-glutamine, and 100 U/mL of penicillin/streptomycin. The third to tenth passages were used for the following cocultivation experiments.

Human breast cancer cells MDA-MB-231 were purchased from American Type Culture Collection (ATCC, Manassas, VA, USA) and cultured in Roswell Park Memorial Institute 1640 medium containing 10% fetal bovine serum, 1 mM sodium pyruvate, 1% nonessential amino acid, 2 mM of L-glutamine, and 100 U/mL of penicillin/streptomycin. All the cells were incubated in a humidified incubator (Thermo Fisher Scientific, Waltham, MA, USA) with 5% CO₂ at 37°C. To simulate the microenvironment of cancer, HUVECs were cocultured with MDA-MB-231 in a transwell coculture system (Merck Millipore, Billerica, MA, USA). HUVECs were seeded in transwell inserts with 0.1 μm pore at a 1:5 ratio to tumor cells and were added into 6-well plates with MDA-MB-231 cultured in them. HUVECs and MDA-MB-231 were all cultured overnight for adherence before cocultivation and maintained in cocultural system for a further 48 hours. The collected cells were called TVECs.

Cytotoxicity analysis

To analyze the biocompatibility of CL-PEG-MnFe₂O₄, we used a Cell Count Kit-8 (CCK-8) to test the cytotoxicity of CL-PEG-MnFe₂O₄ on TVECs in comparison with a molecular manganese agent. Briefly, cells were seeded in 96-well plates at a density of 5×10³ cells/well and cultured overnight. Then, fresh medium containing CL-PEG-MnFe₂O₄ with serial metal (Fe + Mn) concentrations (0, 0.01, 0.05, 0.09, 0.23, 0.45, 0.9, 1.8, and 4.5 mM) and MnCl₂ with serial Mn concentrations (0, 0.01, 0.05, 0.09, 0.23, 0.45, 0.9, 1.8, and 4.5 mM) was added to replace the previous medium and incubated for a further 24 hours, respectively. Each concentration of the samples was repeated five times. Because the CCK-8 assay relies on the optical density of orange formazan and might be affected by the NPs, the medium containing CL-PEG-MnFe₂O₄ and MnCl₂ was displaced by the mixture containing 100 μL of fresh medium and 10 μL of 2-(2-methoxy-4-nitrophenyl)-3-(4-nitrophenyl)-5-(2,4-disulphophenyl)-2H-tetrazolium after incubation for corresponding time. Following 1.5 hours of coculture, the medium containing formazan was transferred into a new 96-well plate with a permanent magnet under the plate to minimize the influence of NPs on the absorbance. A spectral scanning multimode reader (Varioskan Flash, Thermo Scientific) was used to determine the optical density at a wavelength of 490 nm. In addition, for the cytotoxicity assessment of CL-PEG-MnFe₂O₄ on TVECs, the level of intracellular ROS was quantified using a ROS assay kit (Sigma-Aldrich Co.). TVECs were labeled with CL-PEG-MnFe₂O₄ of serial metal concentrations (0, 0.01, 0.05, 0.09, 0.23, 0.45, 0.9, 1.8, and 4.5 mM) for 24 hours. The labeled cells were then incubated

with 2,7-dichlorofluorescein diacetate and the fluorescent intensity was measured by flow cytometry (Moflo XDP, Beckman Coulter, Brea, CA, USA) with excitation and emission wavelengths of 488 and 525 nm, respectively.

Labeling of TVECs

To evaluate the targeted labeling efficiency of CL-PEG-MnFe₂O₄, the TVECs were cocultured with CL-PEG-MnFe₂O₄, PEG-*b*-PCL-MnFe₂O₄, and the mixture of CL-PEG-MnFe₂O₄ and CL 1555 peptides in a ratio of 1:100 (for competition binding experiment) at the same metal concentration of 0.09 mM for 2 hours. Cells incubated with cell medium without any NPs were used as blank control. Prussian blue staining and MRI were used to determine the location within the cells and the labeling rate. For Prussian blue staining, the labeled cells were fixed with 4% paraformaldehyde, incubated with Prussian blue staining solution (containing equal volumes of 2% hydrochloric acid and 2% potassium ferrocyanide) for 30 minutes and stained with neutral red solution for 10 minutes. The images were obtained using an inverted fluorescence microscope (DMIRB, Leica Microsystems, Wetzlar, Germany). For MRI, cells were harvested by trypsinization and resuspended in 0.5 mL of 1% agarose gel in Eppendorf tubes. All the cells were scanned in a head coil using a 3.0 T clinical MR scanner (Signa HDx) following the previous scanning parameters.

Subculture of the labeled cells and their MRI

The TVECs were seeded into cell culture flask with 25 cm² effective area at a density of 4×10⁴ cells/cm². After adherence, the cells were incubated with CL-PEG-MnFe₂O₄ with metal concentration of 0.18 mM for 2 hours. Then, the culture medium with NPs was displaced with fresh medium and the cells were incubated till 80% confluency was reached and tagged as passage one (P₁). Half of labeled TVECs of P₁ were passaged in a 1:2 ratio and tagged as passage two (P₂). The remaining cells were resuspended in 1% agarose gel and scanned in a head coil using a 3.0 T clinical MR scanner according to the parameters described in the section of NP characterization. Similarly, the labeled TVECs were continuously passaged to passage four and each passage was correspondingly tagged as P₃ and P₄ and each passage cell was treated similarly to P₁.

Statistics

All results were expressed as the mean ± standard deviation. Statistical analysis was carried out using SPSS 13.0 software (SPSS Inc., Chicago, IL, USA). The statistical comparisons were performed using the Student's *t*-test and one-way

analysis of variance; a P -value <0.05 indicated a significant difference.

Results

TEM analysis

$MnFe_2O_4$ NPs synthesized from thermal decomposition of iron acetylacetonate and manganese acetylacetonate in a 2:1 ratio were of spheroidal appearance and narrow size distribution (Figure 1A). The results from Image Pro Plus 6.0 showed that the average size was 7.6 ± 1.0 nm (Figure 1B), as counted with 300 NPs that were randomly selected. After being enveloped with amphiphilic block

copolymer PEG-*b*-PCL, dozens of hydrophobic $MnFe_2O_4$ NPs assembled together (Figure 1C). The diameter of PEG-*b*-PCL- $MnFe_2O_4$ was 146.7 ± 25.9 nm according to the TEM photomicrograph (Figure 1D). Figure 2A and B show a high resolution TEM image of a single $MnFe_2O_4$ NP. The spacings between the lattice fringes were measured to be around 0.301 and 0.257 nm, which correspond to the planes of (220) and (311) of bulk $MnFe_2O_4$ very well. Moreover, the measured interplanar spacings based on the diffraction rings in the selected area electron diffraction (inset of Figure 1A) were perfectly in agreement with the respective hkl indexes of bulk $MnFe_2O_4$ from the Joint Committee on Powder Diffraction

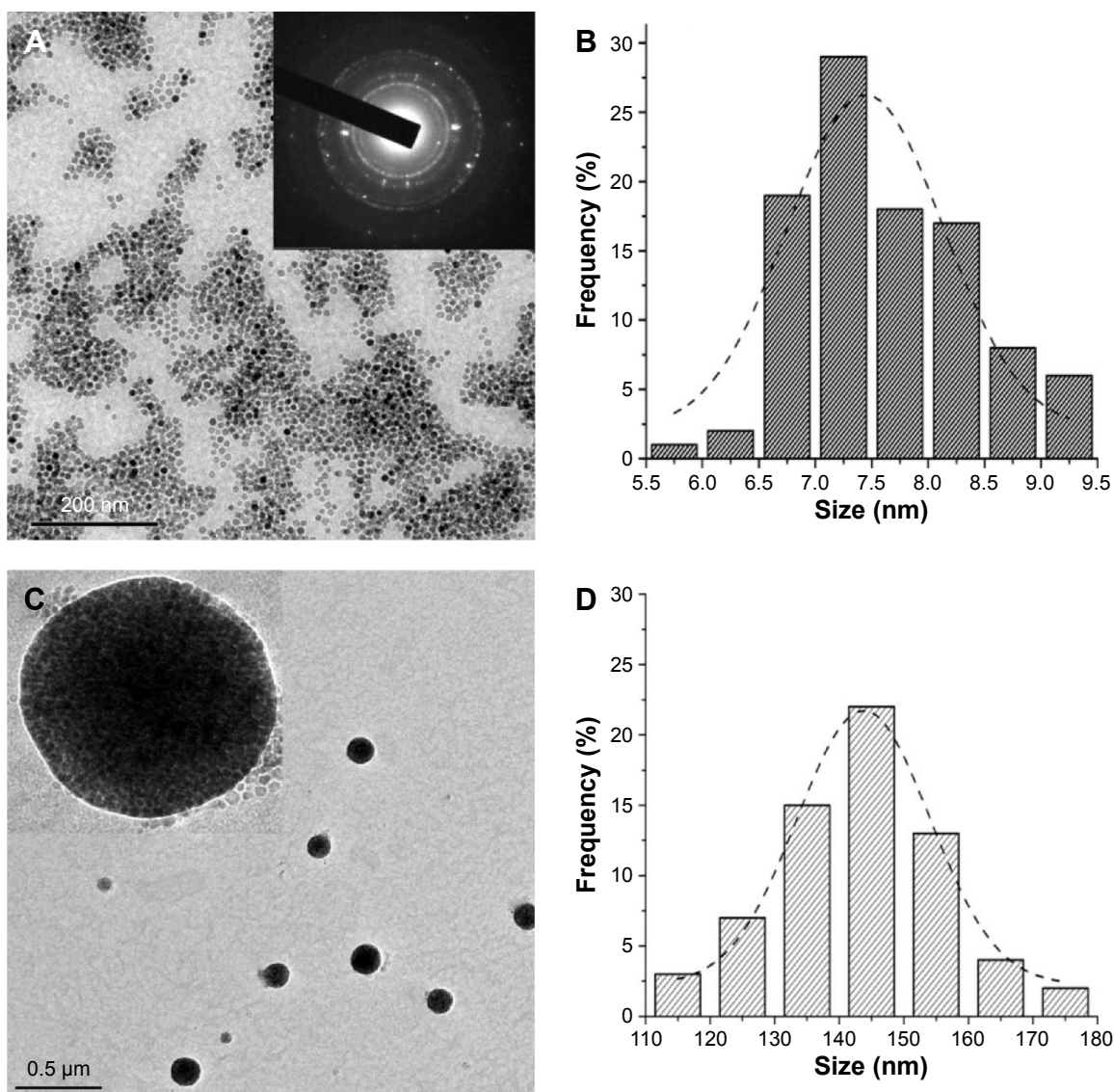


Figure 1 TEM characterization of $MnFe_2O_4$ NPs and PEG-*b*-PCL- $MnFe_2O_4$ NMs.

Notes: $MnFe_2O_4$ NPs were of spheroidal appearance and narrow size distribution (A) and the average size was 7.6 ± 1.0 nm (B). The diameter of PEG-*b*-PCL- $MnFe_2O_4$ NMs was 146.7 ± 25.9 nm (C and D). Inset of (A) is SAED of $MnFe_2O_4$ NPs. Inset of (C) is an enlarged TEM of a single PEG-*b*-PCL- $MnFe_2O_4$ NM; magnification $\times 200,000$.

Abbreviations: NMs, nanomicelles; NPs, nanoparticles; PEG-*b*-PCL, polyethylene glycol-block-poly(ϵ -caprolactone); SAED, selected area electron diffraction; TEM, transmission electron microscopy.

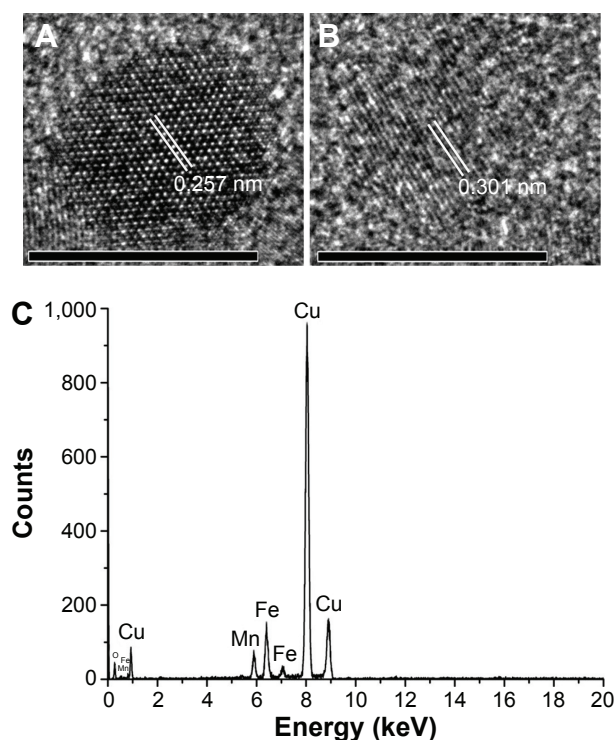


Figure 2 HRTEM and EDS characterization of MnFe_2O_4 NPs.

Notes: HRTEM image of a single MnFe_2O_4 NP showed that the spacing between the lattice fringes of planes (220) and (311) was around 0.257 nm (A) and 0.301 nm (B). The chemical composition of the nanocrystals was confirmed using EDS measurement. EDS (C) of the prepared NPs indicated the presence of Mn, Fe, and O, and the atomic ratio of Fe to Mn was around 2:1. Scale bar = 10 nm.

Abbreviations: EDS, energy dispersive spectrometer; HRTEM, high resolution transmission electron microscopy; NPs, nanoparticles.

Standards (JCPDS) database, indicating that the synthetic NPs are MnFe_2O_4 nanocrystals. The chemical composition of the nanocrystals was confirmed using the energy dispersive spectrometer measurement. The Mn, Fe, and O peaks indicated the presence of Mn, Fe, and O in the NP (Figure 2C); meanwhile, the Cu signal is derived from the TEM grid. The atomic ratio of Fe to Mn was around 2:1, agreeing well with the molar ratio of Fe and Mn in MnFe_2O_4 .

Dynamic light scattering and inductive-coupled plasma optical emission spectrometer measurement

According to the results of dynamic light scattering, the hydrodynamic diameter of MnFe_2O_4 dispersed in hexane was 10.3 ± 1.2 nm (Figure 3A), which was slightly larger than the size measured by TEM. This might be due to the coating of oleic acid or oleylamine on the outer surface of the NP that could affect the light scattering while it could not be detected under the TEM. Similarly, because of the hydrodynamic size effect and electronic permeability of the PEG-b-PCL, the zeta sizes of PEG-*b*-PCL- MnFe_2O_4 and CL-PEG-*b*-PCL- MnFe_2O_4 were 162.6 ± 28.9 nm (Figure 3B) and 183.4 ± 26.5 nm (Figure 3C), which were larger than those obtained from TEM observations. Inductive-coupled plasma optical emission spectrometer analysis showed that Fe and Mn elemental contents of MnFe_2O_4 were 363.5 and 167.9 mg/L, which matched the result of energy dispersive spectrometer analysis and revealed that the molar ratio of Fe and Mn of MnFe_2O_4 was ~2:1, indicating that the prepared NPs were MnFe_2O_4 .

Magnetization and T_2 relaxivity

To understand the magnetic property of the prepared MnFe_2O_4 NPs, 46.8 mg nanopowder was tested using a vibrating sample magnetometer. The magnetization rose nonlinearly with the increase of applied magnetic field (Figure 4A). The prepared NPs showed no remaining net magnetization in the absence of an external field, which indicated that the MnFe_2O_4 NPs were superparamagnetic at 300 K. Under a powerful magnetic field, NPs will reach their saturation magnetization, which was 68.2 emu/g. Figure 5 shows that TMAH- MnFe_2O_4 NPs and PEG-*b*-PCL- MnFe_2O_4 NMs both exhibited a concentration-dependent signal drop in the GRE T_2^* WI and FSE T_2 -weighted imaging. Their signal

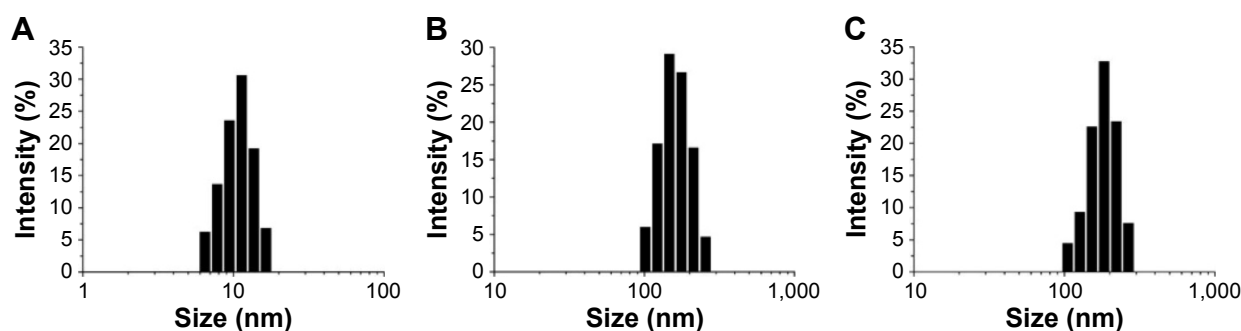


Figure 3 Hydrodynamic diameter of MnFe_2O_4 NPs and NMs.

Notes: The hydrodynamic diameter of MnFe_2O_4 dispersed in hexane was 10.3 ± 1.2 nm (A) and that of PEG-*b*-PCL- MnFe_2O_4 and CL-PEG-*b*-PCL- MnFe_2O_4 was 162.6 ± 28.9 nm (B) and 183.4 ± 26.5 (C), respectively.

Abbreviations: NMs, nanomicelles; NPs, nanoparticles; PEG-*b*-PCL, polyethylene glycol-block-poly(ϵ -caprolactone).

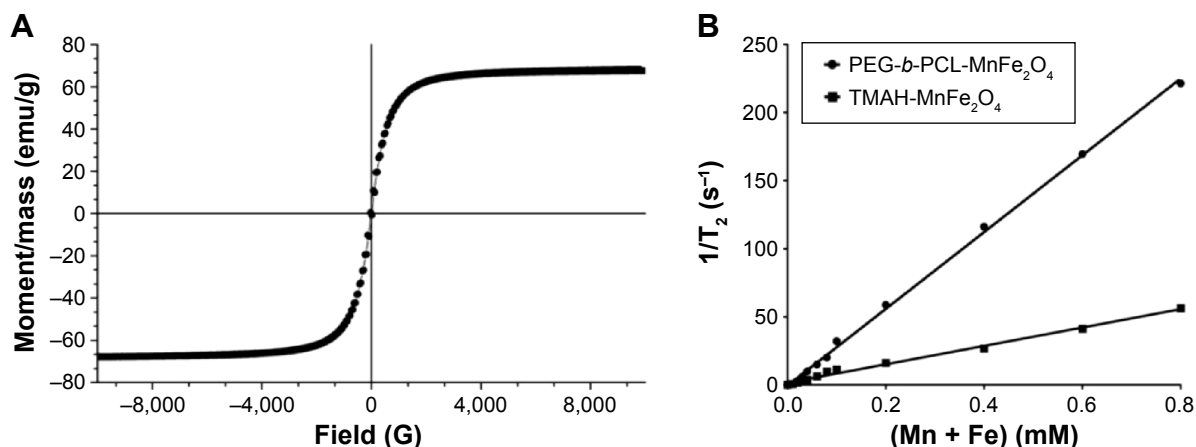


Figure 4 Hysteresis loop and T_2 relaxivity.

Notes: The hysteresis loop of $MnFe_2O_4$ NPs (A) showed that the magnetization rose nonlinearly with the increase of applied magnetic field and no remaining net magnetization in the absence of an external field, indicating that the $MnFe_2O_4$ NPs are superparamagnetic at 300 K. The $MnFe_2O_4$ NPs saturation magnetization was 68.2 emu/g (A). The linear fitting of concentration and $1/T_2$ showed that the r_2 of PEG-*b*-PCL- $MnFe_2O_4$ NMs was $281.7 \text{ mM}^{-1} \text{ s}^{-1}$, which was 4.2 times higher than that of TMAH- $MnFe_2O_4$ NPs ($67.5 \text{ mM}^{-1} \text{ s}^{-1}$) (B).

Abbreviations: NMs, nanomicelles; NPs, nanoparticles; PEG-*b*-PCL, polyethylene glycol-block-poly(ϵ -caprolactone); r_2 , transverse relaxivity; T_2 , transverse relaxation time; TMAH, tetramethylammonium hydroxide.

intensities decreased gradually with the increase of the metal ion concentration. However, PEG-*b*-PCL- $MnFe_2O_4$ NMs induced greater hypointensity at an identical concentration compared with TMAH- $MnFe_2O_4$ NPs. The linear fitting of concentration and $1/T_2$ showed that the r_2 of PEG-*b*-PCL- $MnFe_2O_4$ NMs was $281.7 \text{ mM}^{-1} \text{ s}^{-1}$, which was ~ 4.2 times higher than that of TMAH- $MnFe_2O_4$ NPs ($67.5 \text{ mM}^{-1} \text{ s}^{-1}$) (Figure 4B).

Cytotoxicity analysis

The relative cell viability (RCV) of each treatment group to control group was used to determine the cytotoxicity of CL-PEG- $MnFe_2O_4$ and $MnCl_2$ with different concentrations on TVECs. Figure 6 shows that the RCV of TVECs labeled with CL-PEG- $MnFe_2O_4$ within 0.9 mM decreased only 7%–9% compared to controls. As the concentration increased, the RCV decreased correspondingly, and a decrease of $\sim 19\%$

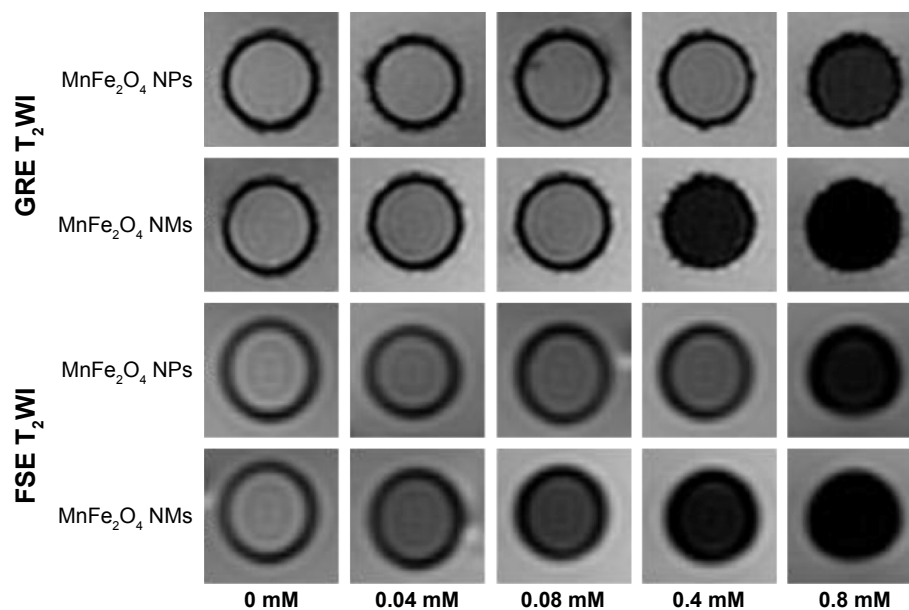


Figure 5 MRI of $MnFe_2O_4$, TMAH- $MnFe_2O_4$ NPs and PEG-*b*-PCL- $MnFe_2O_4$ NMs.

Notes: TMAH- $MnFe_2O_4$ NPs and PEG-*b*-PCL- $MnFe_2O_4$ NMs both exhibited a concentration-dependent signal drop in the GRE T_2 WI and FSE T_2 WI. The signal intensity decreased gradually with the increase of the metal ions concentration, while NMs induced greater hypointensity at an identical concentration compared with NPs.

Abbreviations: MRI, magnetic resonance imaging; NMs, nanomicelles; NPs, nanoparticles; PEG-*b*-PCL, polyethylene glycol-block-poly(ϵ -caprolactone); TMAH, tetramethylammonium hydroxide; T_2 WI, T_2 -weighted imaging; GRE, gradient echo; FSE, fast spin echo.

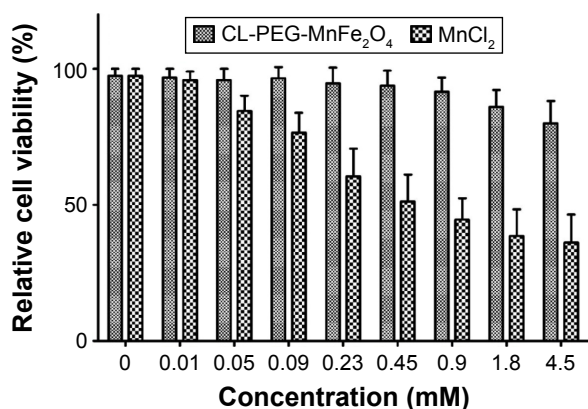


Figure 6 Cytotoxicity analysis.

Notes: The RCV of TVECs labeled with CL-PEG-MnFe₂O₄ within 0.9 mM decreased only 7%–9% compared to controls. As the concentration increased, the RCV decreased correspondingly, and a significant decrease of ~19% in viability of TVECs incubated with 4.5 mM CL-PEG-MnFe₂O₄ solution was measured. On the contrary, a notable decrease of ~15% in viability of TVECs incubated with only 0.05 mM MnCl₂ solution was observed. When the TVECs were incubated with MnCl₂ solution as high as 4.5 mM, there were only 36.2% cells that survived.

Abbreviations: NMs, nanomicelles; PEG, poly(ethylene glycol); RCV, relative cell viability; TVECs, tumor vascular endothelial cells.

in viability of TVECs incubated with 4.5 mM CL-PEG-MnFe₂O₄ solution was measured. On the contrary, a notable decrease of ~15% in viability was observed in TVECs incubated with only 0.05 mM MnCl₂. When the TVECs

were incubated with MnCl₂ solution as high as 4.5 mM, there were only 36.2% cells that survived. The CCK-8 results demonstrated that the CL-PEG-MnFe₂O₄ showed no acute toxicity to TVECs even at high concentrations, indicating their much better biocompatibility than molecular manganese agents. The ROS level of TVECs labeled with 0, 0.05, 0.23, 0.45, 0.9, and 4.5 mM CL-PEG-MnFe₂O₄ solutions are shown in Figure 7. It was shown that the induction of ROS depended on the concentration and an insignificant ROS level elevation was detected in the cells exposed to CL-PEG-MnFe₂O₄ within 0.9 mM. However, a 3.18% higher intracellular ROS level was measured in the cells incubated with 4.5 mM CL-PEG-MnFe₂O₄ solution compared with 0.9 mM CL-PEG-MnFe₂O₄.

Labeling of TVECs with CL-PEG-MnFe₂O₄

As the ferric ferrocyanide, which is a kind of dark blue pigment (also called Prussian blue), can be produced through the reaction of iron with potassium ferrocyanide within the acidic solution, the uptake of the CL-PEG-MnFe₂O₄, PEG-*b*-PCL-MnFe₂O₄, and the mixture of CL-PEG-MnFe₂O₄ and CL 1555 peptides can be observed under optical microscope after Prussian blue staining. Figure 8A–D are the results

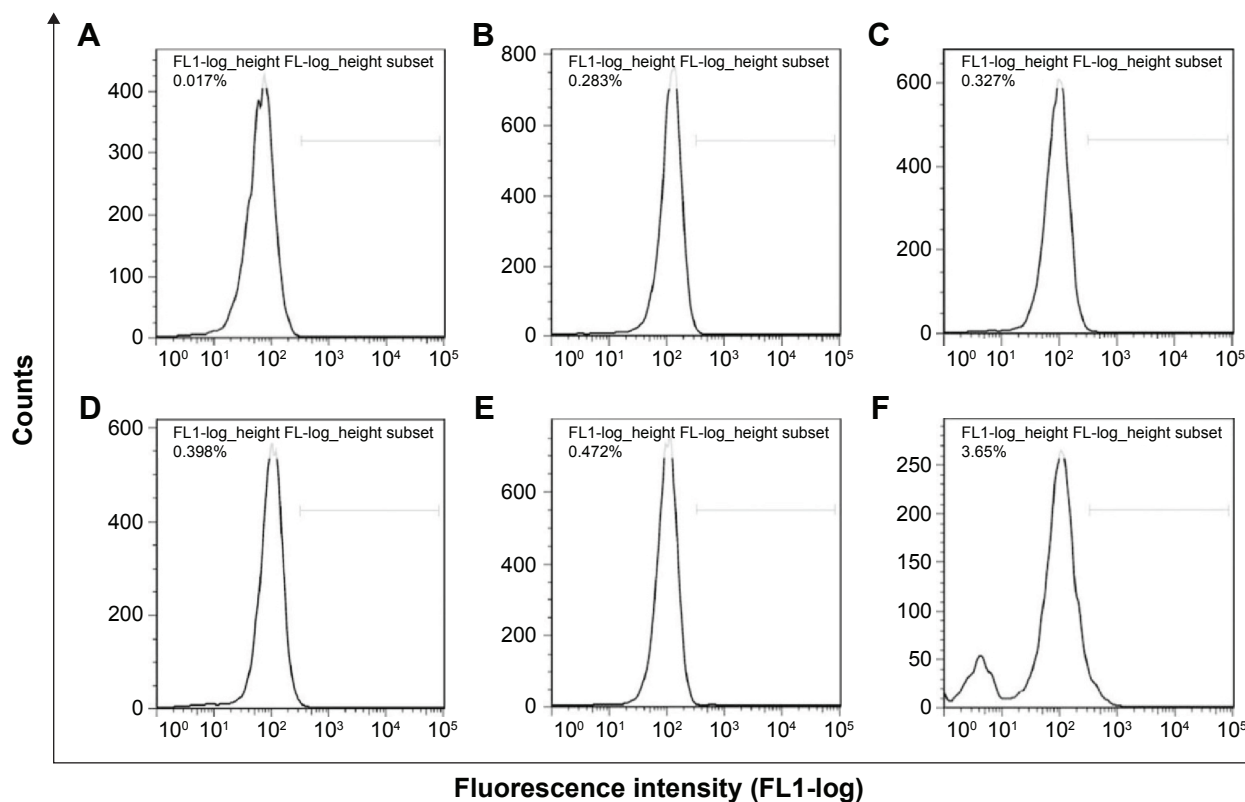


Figure 7 ROS of TVECs labeled with CL-PEG-MnFe₂O₄.

Notes: The ROS levels of TVECs labeled with 0.05 (B), 0.23 (C), 0.45 (D), and 0.9 (E) mM CL-PEG-MnFe₂O₄ solutions were very low and depicted an insignificant elevation of ROS level compared with the control (A). However, a 3.18% higher intracellular ROS level was measured in the cells incubated with 4.5 mM CL-PEG-MnFe₂O₄ solution compared with 0.9 mM CL-PEG-MnFe₂O₄ (F).

Abbreviations: PEG, poly(ethylene glycol); ROS, reactive oxygen species; TVECs, tumor vascular endothelial cells.

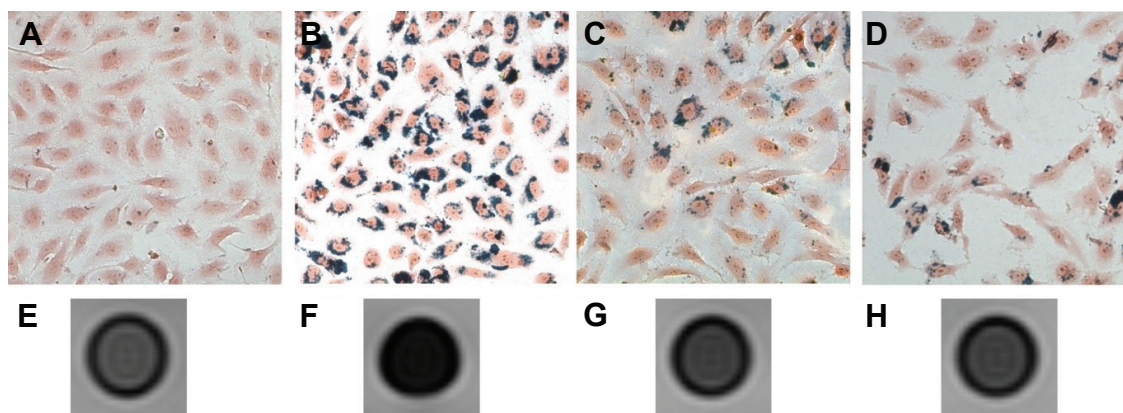


Figure 8 In vitro labeling of TVECs with CL-PEG-MnFe₂O₄.

Notes: Prussian blue staining (200 \times) of control group (A), TVECs labeled with CL-PEG-MnFe₂O₄ (B), PEG-*b*-PCL-MnFe₂O₄ (C) and the mixture of CL-PEG-MnFe₂O₄ and CL 1555 peptides (D). It showed that the uptake of CL-PEG-MnFe₂O₄ was high, while few PEG-*b*-PCL-MnFe₂O₄ was engulfed into TVECs. Blocking CD105 with the free CL 1555 peptides also effectively reduced the amount of blue granules in the cytoplasm of TVECs. (E–H) showed the T₂-weighted MR images of the four groups of cells. Correspondingly, the cells co-cultured with CL-PEG-MnFe₂O₄ (F) showed a more noticeable signal intensity drop than that with PEG-*b*-PCL-MnFe₂O₄ (G) and blocking with the free CL 1555 peptides (H).

Abbreviations: MR, magnetic resonance; PEG-*b*-PCL, polyethylene glycol-block-poly(ϵ -caprolactone); TVECs, tumor vascular endothelial cells.

of Prussian blue staining of control group (Figure 8A) and TVECs labeled with CL-PEG-MnFe₂O₄ (Figure 8B), PEG-*b*-PCL-MnFe₂O₄ (Figure 8C) and the mixture of CL-PEG-MnFe₂O₄ and CL 1555 peptides (Figure 8D), which clearly shows a higher uptake of CL-PEG-MnFe₂O₄ than PEG-*b*-PCL-MnFe₂O₄ into TVECs. Blocking CD105 with the free CL 1555 peptides effectively reduced the amount of blue granules in the cytoplasm of TVECs, indicating that the internalization of CL-PEG-MnFe₂O₄ was specifically mediated by CL 1555 peptides. Figure 8E–H shows the MR images of the four groups of cells. Compared with the control, the cells cocultured with CL-PEG-MnFe₂O₄ showed a noticeable signal intensity drop and its T₂ relaxation time was 38.3 \pm 3.5 ms. However, the cells treated with PEG-*b*-PCL-MnFe₂O₄ and the mixture of CL-PEG-MnFe₂O₄ and CL 1555 peptides showed a similar signal intensity and T₂ relaxation time to the control.

Subculture of the labeled cells and their MRI

The TVECs labeled with CL-PEG-MnFe₂O₄ were subcultured from P₁ to P₄ and each generation was evaluated with a 3.0 T MRI system. As shown in Figure 9, the signal intensity from P₁ to P₄ in T₂-weighted images gradually increased and P₄ had almost equal signal intensity with control group. However, the signal intensity firstly increased and then decreased in T₁-weighted images. The labeled cells of P₁ presented low signal intensity similar to the control and those of P₂, P₃, and P₄ were hyper-intense. The T₁ relaxation time from P₁ to P₄ decreased firstly and then increased back accordingly (Figure 9).

Discussion

Angiogenesis, the formation of new blood vessels, is a requirement for tumor growth and metastasis.^{3,4,43} Moreover, the tumor microvascular density was positively correlated with the trend of tumor metastasis and high microvascular density always leads to poor prognosis.^{44,45} Commonly, the angiogenesis is estimated with histopathological examination. However, histopathological examination for angiogenesis does not demonstrate functionality within the vessels sampled and is inherent invasive and suffers from sampling bias.^{46,47} Molecular imaging targeting vascular endothelial cells can offer this in a noninvasive way.^{46,48–50} Due to a relatively good spatial resolution, good soft-tissue contrast, absence of ionizing radiation, and limited side effects, MRI

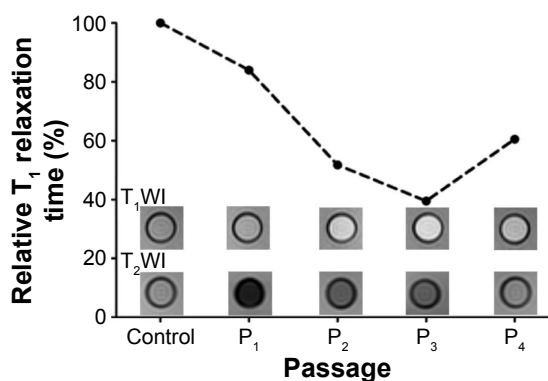


Figure 9 MRI of subcultured labeled TVECs.

Notes: MRI showed that the signal intensity from P₁ to P₄ in T₂WI gradually increased and P₄ had almost equal signal intensity with control group. In T₁WI, the signal intensity from P₁ to P₃ gradually increased and that of P₄ came down to the control. The plot showed that the T₁ relaxation time from P₁ to P₄ decreased firstly and then increased back.

Abbreviations: MRI, magnetic resonance imaging; T₁WI, T₁-weighted imaging; T₂WI, T₂-weighted imaging; TVECs, tumor vascular endothelial cells.

has been proposed to be a good candidate for angiogenesis imaging.^{51–53}

Endoglin, also called CD105, is a 180 kDa transmembrane protein and consists of a homodimer with disulfide links, and it has been found that its expression is usually low in resting endothelial cells and becomes highly expressed once neoangiogenesis begins.^{7,9,54} The important role that CD105 plays in tumor angiogenesis makes it an ideal candidate for tumor targeting imaging. In previous studies, we conjugated anti-CD105 antibody with SL-encapsulated Gd-DTPA and thiol-PEG-carboxyl-stabilized Fe₂O₃/Au NPs to evaluate tumor angiogenesis on T₁- or T₂-enhanced MRI, respectively.^{36,37} The results showed that CD105-Gd-SLs and hybrid-PEG-CD105 could be utilized to detect subcutaneous glioma and breast cancer angiogenesis in tumor-bearing rats. However, because of the larger molecular weight of anti-CD105 antibody, the probes have low connection efficiency and consequently have not enough affinity for the targeted TVECs. In order to improve the affinity of the probes, we employed a peptide – CL 1555 – which consisted of only 12 amino acids as the targeting molecule in the present study. CL 1555 was selected from a phage displayed library and was demonstrated to be of high affinity and selectivity toward CD105.^{33,34} Compared with anti-CD105 antibody, CL 1555 had a lower molecular weight and much smaller steric hindrance, resulting in a high grafting rate on the surface of the NMs. The results of our study showed that compared with PEG-MnFe₂O₄, CL-PEG-MnFe₂O₄ binds to the surface of TVECs much better and markedly shortens T₂ of the labeled TVCEs in T₂-weighted images. In a competition binding experiment, the binding of CL-PEG-MnFe₂O₄ and TVECs was blocked by free CL 1555 peptides, which revealed that the immobilization CL-PEG-MnFe₂O₄ on the surface of TVECs was mediated by CL 1555. So, it was undoubtedly confirmed that CL 1555 was an ideal ligand to CD105 for targeted diagnosis and therapy.

Because of good biocompatibility, superparamagnetic Fe₃O₄ NPs have been widely used as a negative CA for enhanced MRI.^{37,55,56} However, the r_2 of nanoscale Fe₃O₄ was low and not enough for cell imaging and neovessel visualization in the early stage. MnFe₂O₄ NPs have been proven to be of a higher saturation magnetization (M_p) and r_2 than other ferrite NPs, including CoFe₂O₄, Fe₃O₄, and NiFe₂O₄.^{17,57} Lee et al²⁵ fabricated a series of ferrite NPs, including CoFe₂O₄, Fe₃O₄, MnFe₂O₄, and NiFe₂O₄, and investigated their magnetic properties. They found that these ferrite NPs with a size of 12 nm all showed superparamagnetism. However, these NPs with an identical size have different M_p and MnFe₂O₄ exhibited a much higher M_p than CoFe₂O₄,

Fe₃O₄, and NiFe₂O₄. So, we employed MnFe₂O₄ NPs as CAs for TVECs MR molecular imaging in the present study in order to improve the sensitivity of imaging. Besides the M_p , the particle size can also influence the r_2 value. It has been reported that a different relation between r_2 value and particle size follows when the size is within different regimes. When the particles are small, the diffusional motion of water molecules surrounding these NPs is fast enough to average out the magnetic fields induced by these magnetic NPs. This regime is termed as motional averaging and the r_2 value is proportional to $M_p^2 \tau_d$, where τ_d signifies the duration when water protons are under the influence of a magnetic NP and is proportional to r^2/D (D is the diffusion coefficient of water protons). Because τ_d increases with the increase of particle size, the averaging effect diminishes and the magnetic NPs appear as randomly distributed and stationary objects to water protons. In this regime, called static dephasing, the r_2 value is only proportional to M_p . So, increasing the size of individual particle can enhance the r_2 value by motional averaging relaxation.^{17,26,58–61} However, this approach often posed technical difficulties because further increasing the size of the single NP will transfer the magnetic NPs from superparamagnetic to becoming ferromagnetic or ferrimagnetic. Then, the large, single core magnetic NPs will tend to aggregation in suspension because of the magnetic force between each other. An alternative route is to embed multiple magnetic NPs into a single multicore micelle.^{27,62–64} When the NPs aggregate, the size of the single multicore micelle will be increased into static dephasing regime and their r_2 value will be further increased through the static dephasing relaxation mechanism. In this work, we first synthesized the hydrophobic MnFe₂O₄ NPs with a size of ~7.5 nm, which was in the regime of motional averaging. The M_p of the prepared NPs was 68.2 emu/g. Afterward, we transformed the MnFe₂O₄ NPs from hydrophobic to hydrophilic using amphiphilic block copolymer PEG-*b*-PCL. The MnFe₂O₄ NPs modified with PEG-*b*-PCL then self-assembled into clusters and their size increased to ~146.7 nm, which was in the regime of static dephasing. After linear fitting of concentration and $1/T_2$, we found that the clusters consisting of dozens of MnFe₂O₄ NPs were of much higher r_2 of 281.7 mM⁻¹ (Mn + Fe) s⁻¹ than that of single NPs (67.5 mM⁻¹ s⁻¹).

Because these nanoprobe were fabricated for biomedical application, we must evaluate their cytotoxicity first. The in vitro cytotoxicity of CL-PEG-MnFe₂O₄ NMs toward TVECs was evaluated using CCK-8 analysis in comparison with molecular manganese agents. The results showed that the viability of TVECs labeled with CL-PEG-MnFe₂O₄ within 0.9 mM decreased only 7%–9% compared to controls.

As the concentration increased, the RCV decreased correspondingly, and a decrease of ~19% in viability of TVECs incubated with 4.5 mM CL-PEG-MnFe₂O₄ solution was measured. On the contrary, a notable decrease of ~15% in viability was observed in TVECs incubated with only 0.05 mM MnCl₂ solution. When the TVECs were incubated with MnCl₂ solution as high as 4.5 mM, there were only 36.2% cells that survived. So, a conclusion can be easily drawn that the CL-PEG-MnFe₂O₄ showed no acute toxicity to TVECs even at relatively high concentrations, indicating their much better biocompatibility than MnCl₂. Several factors may contribute to the low cytotoxicity of CL-PEG-MnFe₂O₄ NMs. It has been demonstrated that several factors are responsible for the cytotoxicity of NPs, including ROS production and toxic ion leaching.^{65,66} The ROS induction has been posted as one of the main explanations for these toxic effects and induces various deleterious effects, including cell membrane damage, DNA and cytoskeleton injury, autophagy, and apoptosis.⁴² Here, the results of ROS assay depicted that an insignificant ROS level elevation was detected in the cells exposed to CL-PEG-MnFe₂O₄ within 0.9 mM and only a 3.18% higher intracellular ROS level was measured in the cells incubated with 4.5 mM CL-PEG-MnFe₂O₄ solution compared with that incubated with 0.9 mM CL-PEG-MnFe₂O₄, which might explain the CCK-8 results well. Moreover, the ferrite magnetic NPs have been proven to have intrinsic peroxidase-like activity, which can decrease the amount of intracellular H₂O₂ to promote cell proliferation. Regarding the ion leaching, in contrast to MnCl₂ solution, Mn ions leaching from Mn-based NPs have been demonstrated to be slower and Mn-based NPs showed no significant toxic effects on cells at a very high dosage of 200 µg/mL in some previous studies.^{30,31} Actually, to avoid high cytotoxicity of Mn, some researchers employed Mn-based NPs as a sustained release delivery of Mn ions for neuroimaging instead of MnCl₂ solution.^{30,31}

Because of clearance and degradation of NPs from the labeled cells, it was reasonable that the signal intensity from P₁ to P₄ in T₂-weighted MR images gradually increased. However, it was very interesting that the signal intensity of these cells firstly increased and then decreased in T₁-weighted MR images. We hypothesized that T₁ enhancement of the labeled cells resulted from the divalent manganese ions and the smaller size MnFe₂O₄ NPs. It has been observed that the internalized nano- and microparticles are exclusively located within endosomes and finally in the lysosomes.^{30,67} Due to the abundance of proteolytic enzymes, chelating agents, and an acidic environment, the internalized particles will finally be degraded. For MnFe₂O₄ NPs, they were dissolved gradually and metallic

ions Mn²⁺ and Fe³⁺ slowly released. Divalent manganese ions have five unpaired electrons and are paramagnetic, which have been regarded as strong T₁ MRI CAs.³¹ Additionally, the reduction of NP size accompanied with the degradation of MnFe₂O₄ may also contribute to the high signal intensity of P₃ in T₁-weighted MR images. It is known that the surface atom ratio is inversely proportional to the particle size and large particles exhibit lower surface Mn²⁺ ratio, leading to a small longitudinal relaxivity.²⁸ When the internalized MnFe₂O₄ was degraded, its size decreased gradually. Accordingly, the surface Mn²⁺ ratio of MnFe₂O₄ increased rapidly, resulting in a continuous growth of longitudinal relaxivity. When the size is 2.2 nm, the longitudinal relaxivity of MnFe₂O₄ is 6.61 mM⁻¹ s⁻¹, which is higher than that of the clinically used Gd-DTPA agent ($r_1=4.8$ mM⁻¹ s⁻¹).²⁹

Conclusion

In this study, we have successfully prepared an angiogenesis-targeting nanoprobe of high sensitivity for T₁ and T₂ MRI. The nanoprobe consists of MnFe₂O₄ NMs, which act as an MRI CA, and a peptide named CL 1555 for active targeting. These nanoprobes could specifically target TVECs with CD105 expression. The labeled TVECs could be imaged in T₂-weighted MRI and also in T₁-weighted MRI with the passage of labeled cells and the degradation of the internalized NPs. Based on these results, the prepared CL-PEG-MnFe₂O₄ nanoprobe could act as a promising CA for early detection of tumor angiogenesis using targeting T₁- and T₂-enhanced MRI.

Acknowledgments

We are very grateful to the National Natural Science Foundation of China (81401466 and 81501521) and General project of the frontier and application basic research plan of Chongqing (cstc2015jcyjA1338) for financial support.

Disclosure

The authors report no conflicts of interest in this work.

References

1. Torre LA, Bray F, Siegel RL, Ferlay J, Lortet-Tieulent J, Jemal A. Global cancer statistics, 2012. *CA Cancer J Clin*. 2015;65(2):87–108.
2. Morgan-Parkes JH. Metastases: mechanisms, pathways, and cascades. *AJR Am J Roentgenol*. 1995;164(5):1075–1082.
3. Blood CH, Zetter BR. Tumor interactions with the vasculature: angiogenesis and tumor metastasis. *Biochim Biophys Acta*. 1990;1032(1): 89–118.
4. Folkman J, Merler E, Abernathy C, Williams G. Isolation of a tumor factor responsible for angiogenesis. *J Exp Med*. 1971;133(2):275–288.
5. Erber R, Thurnher A, Katsen AD, et al. Combined inhibition of VEGF and PDGF signaling enforces tumor vessel regression by interfering with pericyte-mediated endothelial cell survival mechanisms. *FASEB J*. 2004;18(2):338–340.

6. Brooks PC, Montgomery AM, Rosenfeld M, et al. Integrin $\alpha_v\beta_3$ antagonists promote tumor regression by inducing apoptosis of angiogenic blood vessels. *Cell*. 1994;79(7):1157–1164.
7. Fonsatti E, Altomonte M, Nicotra MR, Natali PG, Maio M. Endoglin (CD105): a powerful therapeutic target on tumor-associated angiogenic blood vessels. *Oncogene*. 2003;22(42):6557–6563.
8. Seon BK. Expression of endoglin (CD105) in tumor blood vessels. *Int J Cancer*. 2002;99(2):310–311.
9. Duff SE, Li C, Garland JM, Kumar S. CD105 is important for angiogenesis: evidence and potential applications. *FASEB J*. 2003;17(9):984–992.
10. Edelman RR, Warach S. Magnetic resonance imaging. *N Engl J Med*. 1993;328(10):708–716.
11. Pichler BJ, Kolb A, Nägele T, Schlemmer H-P. PET/MRI: paving the way for the next generation of clinical multimodality imaging applications. *J Nucl Med*. 2010;51(3):333–336.
12. Thompson WO, Thaete FL, Fu FH, Dye SF. Tibial meniscal dynamics using three-dimensional reconstruction of magnetic resonance images. *Am J Sports Med*. 1991;19(3):210–216.
13. Weissleder R, Mahmood U. Molecular imaging 1. *Radiology*. 2001;219(2):316–333.
14. Satoh Y, Ichikawa T, Motosugi U, et al. Diagnosis of peritoneal dissemination: comparison of ^{18}F -FDG PET/CT, diffusion-weighted MRI, and contrast-enhanced MDCT. *AMJ Am J Roentgenol*. 2011;196(2):447–453.
15. Hu B, Dai F, Fan Z, Ma G, Tang Q, Zhang X. Nanotheranostics: Congo Red/Rutin-MNPs with enhanced magnetic resonance imaging and H_2O_2 -responsive therapy of Alzheimer's disease in APPswe/PS1dE9 transgenic mice. *Adv Mater*. 2015;27(37):5499–5505.
16. Galdes CF, Laurent S. Classification and basic properties of contrast agents for magnetic resonance imaging. *Contrast Media Mol Imaging*. 2009;4(1):1–23.
17. Tromsdorf UI, Bigall NC, Kaul MG, et al. Size and surface effects on the MRI relaxivity of manganese ferrite nanoparticle contrast agents. *Nano Lett*. 2007;7(8):2422–2427.
18. Hong S, Chang Y, Rhee I. Chitosan-coated ferrite (Fe_3O_4) nanoparticles as a T_2 contrast agent for magnetic resonance imaging. *J Korean Phys Soc*. 2010;56(3):868–873.
19. Leal MP, Rivera-Fernández S, Franco JM, Pozo D, Jesús M, García-Martin ML. Long-circulating PEGylated manganese ferrite nanoparticles for MRI-based molecular imaging. *Nanoscale*. 2015;7(5):2050–2059.
20. Bae KH, Kim YB, Lee Y, Hwang J, Park H, Park TG. Bioinspired synthesis and characterization of gadolinium-labeled magnetite nanoparticles for dual contrast T_1 - and T_2 -weighted magnetic resonance imaging. *Bioconjug Chem*. 2010;21(3):505–512.
21. Hu F, Jia Q, Li Y, Gao M. Facile synthesis of ultrasmall PEGylated iron oxide nanoparticles for dual-contrast T_1 - and T_2 -weighted magnetic resonance imaging. *Nanotechnology*. 2011;22(24):245604.
22. High WA, Ayers RA, Cowper SE. Gadolinium is quantifiable within the tissue of patients with nephrogenic systemic fibrosis. *J Am Acad Dermatol*. 2007;56(4):710–712.
23. Song Q, Zhang ZJ. Controlled synthesis and magnetic properties of bimagnetic spinel ferrite CoFe_2O_4 and MnFe_2O_4 nanocrystals with core-shell architecture. *J Am Chem Soc*. 2012;134(24):10182–10190.
24. Xu C, Sun S. New forms of superparamagnetic nanoparticles for biomedical applications. *Adv Drug Deliv Rev*. 2013;65(5):732–743.
25. Lee JH, Huh YM, Jun YW, et al. Artificially engineered magnetic nanoparticles for ultra-sensitive molecular imaging. *Nat Med*. 2007;13(1):95–99.
26. Lee H, Shin TH, Cheon J, Weissleder R. Recent developments in magnetic diagnostic systems. *Chem Rev*. 2015;115(19):10690–10724.
27. Yoon T-J, Lee H, Shao H, Hilderbrand SA, Weissleder R. Multicore assemblies potentiate magnetic properties of biomagnetic nanoparticles. *Adv Mater*. 2011;23(41):4793–4797.
28. Niu D, Luo X, Li Y, Liu X, Wang X, Shi J. Manganese-loaded dual-mesoporous silica spheres for efficient T_1 - and T_2 -weighted dual mode magnetic resonance imaging. *ACS Appl Mater Interfaces*. 2013;5(20):9942–9948.
29. Li Z, Wang SX, Sun Q, et al. Ultrasmall manganese ferrite nanoparticles as positive contrast agent for magnetic resonance imaging. *Adv Healthc Mater*. 2013;2(7):958–964.
30. Shapiro EM, Koretsky AP. Convertible manganese contrast for molecular and cellular MRI. *Magn Reson Med*. 2008;60(2):265–269.
31. Chen W, Lu F, Chen CC, et al. Manganese-enhanced MRI of rat brain based on slow cerebral delivery of manganese(II) with silica-encapsulated $\text{Mn}_x\text{Fe}_{1-x}\text{O}$ nanoparticles. *NMR Biomed*. 2013;26(9):1176–1185.
32. Chen F-Y, Gu Z-J, Wan H-P, Xu X-Z, Tang Q. Manganese nanosystem for new generation of MRI contrast agent. *Rev Nanosci Nanotechnol*. 2015;4(2):81–91.
33. Bi X, Liang Z, Shi L. Determination of functional affinity of rhEndoglin conjugated peptide. *J Third Mil Med Univ*. 2007;29(8):685–687.
34. Bi X, Liang Z, Shi L. Screening and function analysis of targeted short binding peptides of endoglin. *J Chongqing Medical Univ*. 2007;32(3):232–235.
35. Ghosh P, Han G, De M, Kim CK, Rotello VM. Gold nanoparticles in delivery applications. *Adv Drug Deliv Rev*. 2008;60(11):1307–1315.
36. Zhang D, Feng XY, Henning TD, et al. MR imaging of tumor angiogenesis using sterically stabilized Gd-DTPA liposomes targeted to CD105. *Eur J Radiol*. 2009;70(1):180–189.
37. Zhang S, Gong M, Zhang D, Yang H, Gao F, Zou L. Thiol-PEG-carboxyl-stabilized $\text{Fe}_2\text{O}_3/\text{Au}$ nanoparticles targeted to CD105: Synthesis, characterization and application in MR imaging of tumor angiogenesis. *Eur J Radiol*. 2014;83(7):1190–1198.
38. Sun S, Zeng H, Robinson DB, et al. Monodisperse MFe_2O_4 ($\text{M} = \text{Fe}, \text{Co}, \text{Mn}$) nanoparticles. *J Am Chem Soc*. 2004;126(1):273–279.
39. Lim J, Eggeman A, Lanni F, Tilton RD, Majetich SA. Synthesis and single-particle optical detection of low-polydispersity plasmonic-superparamagnetic nanoparticles. *Adv Mater*. 2008;20(9):1721–1726.
40. Farokhzad OC, Jon S, Khademhosseini A, Tran TN, Lavan DA, Langer R. Nanoparticle-aptamer bioconjugates: a new approach for targeting prostate cancer cells. *Cancer Res*. 2004;64(21):7668–7672.
41. Farokhzad OC, Cheng J, Tepley BA, et al. Targeted nanoparticle-aptamer bioconjugates for cancer chemotherapy in vivo. *Proc Natl Acad Sci U S A*. 2006;103(16):6315–6320.
42. Gong M, Yang H, Zhang S, et al. Superparamagnetic core/shell Gold-Mag nanoparticles: size-, concentration- and time-dependent cellular nanotoxicity on human umbilical vein endothelial cells and the suitable conditions for magnetic resonance imaging. *J Nanobiotechnology*. 2015;13:24.
43. O'Reilly MS, Boehm T, Shing Y, et al. Endostatin: An endogenous inhibitor of angiogenesis and tumor growth. *Cell*. 1997;88(2):277–285.
44. Jackson A, Kassner A, Annesley-Williams D, Reid H, Zhu X-P, Li K-L. Abnormalities in the recirculation phase of contrast agent bolus passage in cerebral gliomas: comparison with relative blood volume and tumor grade. *Am J Neuroradiol*. 2002;23(1):7–14.
45. Strohmeier D, Rössing C, Strauss F, Bauerfeind A, Kaufmann O, Loening S. Tumor angiogenesis is associated with progression after radical prostatectomy in pT2/pT3 prostate cancer. *Prostate*. 2000;42(1):26–33.
46. Barrett T, Kobayashi H, Brechbiel M, Choyke PL. Macromolecular MRI contrast agents for imaging tumor angiogenesis. *Eur J Radiol*. 2006;60(3):353–366.
47. Barrett T, Brechbiel M, Bernardo M, Choyke PL. MRI of tumor angiogenesis. *J Magn Reson Imaging*. 2007;26(2):235–249.
48. Samei E, Saunders RS, Badea CT, et al. Micro-CT imaging of breast tumors in rodents using a liposomal, nanoparticle contrast agent. *Int J Nanomedicine*. 2009;4:277–282.

49. Liu Y, Yang Y, Zhang C. A concise review of magnetic resonance molecular imaging of tumor angiogenesis by targeting integrin $\alpha_v\beta_3$ with magnetic probes. *Int J Nanomedicine*. 2013;8:1083–1093.
50. Key J, Leary JF. Nanoparticles for multimodal in vivo imaging in nanomedicine. *Int J Nanomedicine*. 2014;9:711–726.
51. Wong EC. Vessel-encoded arterial spin-labeling using pseudocontinuous tagging. *Magn Reson Med*. 2007;58(6):1086–1091.
52. Li SP, Padhani AR, Makris A. Dynamic contrast-enhanced magnetic resonance imaging and blood oxygenation level-dependent magnetic resonance imaging for the assessment of changes in tumor biology with treatment. *J Natl Cancer Inst Monogr*. 2010;2011(43):103–107.
53. Hayes C, Padhani AR, Leach MO. Assessing changes in tumour vascular function using dynamic contrast-enhanced magnetic resonance imaging. *NMR Biomed*. 2002;15(2):154–163.
54. Clara CA, Marie SK, de Almeida JR, et al. Angiogenesis and expression of PDGF-C, VEGF, CD105 and HIF-1 α in human glioblastoma. *Neuropathology*. 2014;34(4):343–352.
55. Xie J, Xu C, Kohler N, Hou Y, Sun S. Controlled PEGylation of monodisperse Fe₃O₄ nanoparticles for reduced non-specific uptake by macrophage cells. *Adv Mater*. 2007;19(20):3163–3166.
56. Ling D, Lee N, Hyeon T. Chemical synthesis and assembly of uniformly sized iron oxide nanoparticles for medical applications. *Acc Chem Res*. 2015;48(5):1276–1285.
57. Mazarío E, Sánchez-Marcos J, Menéndez N, et al. High specific absorption rate and transverse relaxivity effects in manganese ferrite nanoparticles obtained by an electrochemical route. *J Phys Chem C*. 2015;119(12):6828–6834.
58. Chouly C, Pouliquen D, Lucet I, Jeune J, Jallet P. Development of superparamagnetic nanoparticles for MRI: effect of particle size, charge and surface nature on biodistribution. *J Microencapsul*. 1996;13(3):245–255.
59. Duan H, Kuang M, Wang X, Wang YA, Mao H, Nie S. Reexamining the effects of particle size and surface chemistry on the magnetic properties of iron oxide nanocrystals: new insights into spin disorder and proton relaxivity. *J Phys Chem C*. 2008;112(22):8127–8131.
60. Yablonskiy DA, Haacke EM. Theory of NMR signal behavior in magnetically inhomogeneous tissues: the static dephasing regime. *Magn Reson Med*. 1994;32(6):749–763.
61. Brooks RA. T₂-shortening by strongly magnetized spheres: A chemical exchange model. *Magn Reson Med*. 2002;47(2):388–391.
62. Lu J, Ma S, Sun J, et al. Manganese ferrite nanoparticle micellar nanocomposites as MRI contrast agent for liver imaging. *Biomaterials*. 2009;30(15):2919–2928.
63. Ge J, Hu Y, Biasini M, Beyermann WP, Yin Y. Superparamagnetic magnetite colloidal nanocrystal clusters. *Angew Chem Int Ed Engl*. 2007;46(23):4342–4345.
64. Roca AG, Veintemillas-Verdaguer S, Port M, Robic C, Serna CJ, Morales MP. Effect of nanoparticle and aggregate size on the relaxometric properties of MR contrast agents based on high quality magnetite nanoparticles. *J Phys Chem B*. 2009;113(19):7033–7039.
65. Nel A, Xia T, Mädler L, Li N. Toxic potential of materials at the nanolevel. *Science*. 2006;311(5761):622–627.
66. Soenen SJ, Manshian B, Montenegro JM, et al. Cytotoxic effects of gold nanoparticles: a multiparametric study. *ACS Nano*. 2012;6(7):5767–5783.
67. Arbab AS, Wilson LB, Ashari P, Jordan EK, Lewis BK, Frank JA. A model of lysosomal metabolism of dextran coated superparamagnetic iron oxide (SPIO) nanoparticles: implications for cellular magnetic resonance imaging. *NMR Biomed*. 2005;18(6):383–389.

International Journal of Nanomedicine

Publish your work in this journal

The International Journal of Nanomedicine is an international, peer-reviewed journal focusing on the application of nanotechnology in diagnostics, therapeutics, and drug delivery systems throughout the biomedical field. This journal is indexed on PubMed Central, MedLine, CAS, SciSearch®, Current Contents®/Clinical Medicine,

Submit your manuscript here: <http://www.dovepress.com/international-journal-of-nanomedicine-journal>

Dovepress

Journal Citation Reports/Science Edition, EMBase, Scopus and the Elsevier Bibliographic databases. The manuscript management system is completely online and includes a very quick and fair peer-review system, which is all easy to use. Visit <http://www.dovepress.com/testimonials.php> to read real quotes from published authors.